Article

The Role of the Precursor on the Electrochemical Performance of N,S Co-Doped Graphene Electrodes in Aqueous Electrolytes

Rodrigo Braga [1,*], Diana M. Fernandes [2], Alberto Adán-Más [1,3], Teresa M. Silva [4] and M. F. Montemor [1,*]

1 Centro de Química Estrutural-CQE, Institute of Molecular Sciences, Departamento Engenharia Química, Instituto Superior Técnico, Universidade de Lisboa, 1049-001 Lisboa, Portugal
2 REQUIMTE-LAQV/Departamento de Química e Bioquímica, Faculdade de Ciências, Universidade do Porto, 4169-007 Porto, Portugal
3 C2CNewCap Av. José Francisco Guerreiro, Paiã Park, Armazém A2.12, 1675-078 Odivelas, Portugal
4 Departamento de Engenharia Mecânica, GI-MOSM, Instituto Superior de Engenharia de Lisboa—ISEL, 1950-062 Lisboa, Portugal
* Correspondence: rodrigo.braga@tecnico.ulisboa.pt (R.B.); mfmontemor@tecnico.ulisboa.pt (M.F.M.)

Abstract: The introduction of pillared agents or dopants to the graphene used as the electroactive material in supercapacitor electrodes can be an efficient way to facilitate ion transfer, mitigate re-stacking, and improve electrochemical performance. We evaluated the effect of different precursors containing nitrogen (N) and sulfur (S) atoms to dope graphene flake (GF) lattices. The electrochemical performance of the doped GF was assessed in 1 M KOH and 1 M Na_2SO_4 electrolytes. N- and S-doped GF flakes were synthesized via mechanochemical synthesis, also known as ball milling. After being ground, the materials were calcined under N_2. The physicochemical characterization of the materials evidenced the co-doping of both S and N into the graphene backbone, as corroborated by the results of Raman spectroscopy, X-ray diffraction (XRD), X-ray photoelectron spectroscopy (XPS), and transmission electron microscopy (TEM). As shown by the results, the nature of the precursors influences the ratio of S and N in the doped graphene flakes and, consequently, the response of the electroactive electrode material. The co-doping obtained using 4-amino-3-hydrazino-5-mercapto-1,2,4-triazole revealed a specific capacitance of 48 F.g^{-1} at 1.0 A·g^{-1} and over 90% capacitance retention after 10,000 cycles at 10.0 A·g^{-1} in Na_2SO_4.

Keywords: nitrogen/sulfur-doped graphene; ball milling; electrodes; supercapacitor

1. Introduction

The growing demand for renewable energy and sustainable energy management solutions is increasing the interest in energy harvesting with electrical energy storage systems (EESs) using, for example, batteries and supercapacitors [1]. Over the past years, supercapacitors, or electric double-layer capacitors (EDLCs), have been intensively studied as EESs for peak-power applications because of their characteristic features, namely long cycle life, high stability under cycling, and remarkable power density [2,3]. The applications of supercapacitor devices are increasing, one of which is related to current supercapacitors displaying very low energy density, which limits their applicability in certain situations [4]. As consequence, there is increasing interest in developing novel electrode compositions to expand the execution of carbon-based electrodes for supercapacitors.

Doped-carbon-based materials, with large active surface areas, have the potential for reaching higher energy densities at high power with stable cycling performance [5]. Amid the carbonaceous materials commonly utilized in EDLCs, for instance, activated carbon [6], carbon fibers [7], or carbon nanotubes [8], graphene has attracted immense interest over the past years. Being a 2D material, graphene shows remarkable electrical conductivity, competitive specific capacitance, as well as large specific surface area (SSA) [9,10]. However, pure graphene still shows modest specific capacitance and, therefore, low energy density.

A strategy to improve the electrochemical performance of graphene involves modification through the insertion of components via heteroatom doping [11]. The literature shows that doping is a promising strategy to enhance chemical reactivity and electron transfer kinetics [12]. The insertion of functional groups onto graphene's surface increases electroconductivity and surface wettability, and provides other benefits [13]. For example, 2,5-dimercapto-1,3,4-thiadiazole (DMTD) prevents graphene from stacking due to the resulting ring planar molecule with N, S that establishes covalent bonds with C [14]. Urea is another typical organic compound that participates in the loading of heteroatoms onto carbon lattices, bettering its functionalities by modifying the electronic features of carbon and changing the fermi level to the conduction band [15]. Other chemical compounds that include N and S heteroatoms in their structure are also emerging for constructing dual-doped graphene displaying functional groups. Likewise, those compounds contribute to simpler doping methods [16]. 1,3,5-triazine-2,4,6-trithiol (trithiocyanuric acid) is another compound that has been used to modify graphene oxide (GO) for electrochemical applications [17]. This compound is very reactive and possesses a symmetric structure containing reactive elements, i.e., three N and three S atoms [17]. Sulfur (100 pm, atomic radius) and nitrogen (70 pm) atoms can interact with the graphene lattice (C, 65 pm), contributing to modifying the properties of the original material.

Other elements, such as boron (B) and phosphorus (P), can also be introduced as dopants producing functional groups during the synthesis of graphene without losing the specific surface area (SSA) and acting as faradaic sites, subsequently favoring reactions [18,19]. These dopants, which can either be molecular structures or individual atoms, can also replace or create covalent bonds with carbon (C) atoms [20]. However, nitrogen is commonly used in carbon-based structures to enhance the electrode/electrolyte interactions. Nitrogen has electrons in its valence shell, resulting in an atom size equivalent to that of carbon, thus facilitating C–N bonding [20]. Moreover, N groups can introduce pseudocapacitive properties into graphene frameworks, contributing to higher electronic conductivity and better wettability of the electrode surface [21]. As a consequence, electrodes made using N-doped carbons display increased energy density owing to enhanced mass transfer and a pseudocapacitive contribution to ameliorating the issues experienced with electrode materials [22,23].

The presence of both N and S may create a synergistic contribution that enhances the electrochemical response of doped graphene electrodes due to the combined electronegativity of N (3.04) and S (2.55) [18]. Investigations proved that the adsorption of multiple heteroatoms can improve the electron transfer of graphene [24]. It was reported that sulfur (S) can contribute to maintaining the spacing between graphene layers while favoring the reaction kinetics [25]. Additionally, sulfur can introduce additional active sites into the graphene surface, facilitating electrode–electrolyte interactions. It also enhances electroconductivity [26] through sulfur-thiophene-like and sulfone arrangements [27]. Interestingly, nitrogen functionalities bring three different types of bonds to the S/N-doped graphene backbone. One of them, pyridine N (sp^2 hybridization) greatly improves the ion attraction, forming two bonds with C and one with O on graphene edges or defects. Another one, pyrrolic N (sp^3 hybridization) upgrades the wettability of the material in an aqueous electrolyte. The third one, graphitic N or (quaternary N), sp^2 hybridization, facilitates electron transfer and holds the capacitance stability at higher current densities [27,28].

Chen et al. [29] studied EMIMBF$_4$ ionic liquid electrolytes, finding that graphene doping by hydrazine and sulfur introduces different N functionalities and S groups that enhance electronic conductivity. Another study by Fujisawa et al. [30] involved dual-doped graphene oxide in a rich boron (B) environment and nitrogen plasma. The study was carried out in alkaline (6 M KOH) and acidic (1 M H$_2$SO$_4$) electrolytes; the maximum specific gravimetric capacitance was 29.6 and 29.7 F·g^{-1}, respectively. Some methods adopted for doping heteroatoms on carbon-based material use multiple steps, for example, mechanical induced sol-gel, carbonization, activation, and pyrolysis methods [15,19]. Despite the various studies conducted in different electrolytes, the outcome of dual doping with N

and S atoms has not been well detailed; in particular, the role of the original S and N precursors on the final response of electrode materials has rarely been discussed. Looking at the literature, the selection of precursors and respective molecular structures has not been guided by systematic studies that describe the rationale of selecting the precursor. The electrochemical performance of S and N precursors on the electrochemical response of electrode materials in aqueous electrolytes has rarely been explored in alkaline and neutral solutions, such as in KOH and Na_2SO_4. These electrolytes are cheap and ecofriendly, have attractive conductivity, and enhance the charge storage capability [31]. This study sheds new light to the role of the N and S precursors on the final performance of double doping onto graphene backbone. The process was achieved by mechanochemical synthesis, also known as ball milling which is a simple, clean, and efficient synthesis route. This is a top-down process that shears larger particles into thin layers using the impact and frictional forces promoted by the spheres. The balls impact the graphene nanosheets, preventing them from stacking, while the Van der Waals forces of the graphene layers are shattered, allowing the impregnation of the heteroatoms as raw materials at the broken edges of the graphene lattice [32,33]. Dopants are introduced by the formation of hydrogen bonds, promoting several points of interactions with the graphene surface [34]. Throughout this method, more active sites emerge, and the active surface area of the bare graphene is enlarged [35]. Recently, ball milling has been considered for the synthesis of graphene because it is simple and economical, uses nontoxic and gentle solvents, and is very efficient in the exfoliation of graphene compared with several other methods of synthesis [36]. Moreover, mechanochemical synthesis allows the testing different types and concentrations of precursors of dopant atoms and is an innovative and clean synthesis route [37].

In the present work, we explored the effect of different precursors containing N and S elements for the first time to create different functional graphene supercapacitor electrodes. The electrochemical measurements of the resulting materials were evaluated in 1 M Na_2SO_4 and 1 M KOH electrolytes.

2. Materials and Methods

Commercial graphene flakes (GFs; Graphene Technologies, Novato, CA, USA, Lot GTX-7/6−10.4.13), 1,3,5-triazine-2,4,6-trithiol (Trithiocyanuric acid, S_3N_3, Sigma-Aldrich, Algés, Portugal), 2-5-dimercapto-1,3,4-thiadiazole (S_3N_2, Sigma-Aldrich, Algés, Portugal), and 4-amino-3-hydrazino-5-mercapto-1,2,4-triazole (SN_6, Sigma-Aldrich, Algés, Portugal) were used as received for materials' preparation.

The mechanosynthesis of different precursors (S, N-doped graphene flake) was carried out using an MM200 Retsch mixer mill (Retsch GMBH, Haan, Germany), without solvents. The milling was performed in a zirconium oxide grinding vessel (25 mL) using balls (2 mm each ball, ≈100 balls made of the same material).

S, N-doped graphene flakes were synthesized by mixing GFs (400 mg) with the suitable precursor (SN_6, S_3N_3, or S_3N_2) in the desired proportion (25:75) to obtain crushed, exfoliated, and thin nanosheets, as depicted in Table 1, which we milled for 5 h at a constant vibrational frequency (15 Hz) to achieve the effective ratio of dopants incorporated in the graphene network. After ball milling, the material was subjected to heat treatment at 800 °C under an inert atmosphere (N_2) for 1 h to attain the beneficial nitrogen functionalities [38,39]. The resulting materials were labeled SN_6_GF, S_3N_3_GF, and S_3N_2_GF [40], which were used as electrode materials.

Table 1. Description of the different precursor materials used in this work.

Material	Precursor
SN_6_GF	4-amino-3-hydrazino-5-mercapto-1,2,4-triazole ($C_2H_6N_6S$)
S_3N_3_GF	1,3,5-triazine-2,4,6-trithiol ($C_3H_3N_3S_3$)
S_3N_2_GF	2-5-dimercapto-1,3,4-thiadiazole ($C_2H_2N_2S_3$)

Raman spectra were obtained on a Jobin Yvon HR800 apparatus (Horiba, Japan) at 532 nm; X-ray photoelectron spectroscopy (XPS) studies were carried out using a VG Scientific ESCALAB 200A apparatus. The nanostructure of S, N-doped graphene flakes was studied by high-resolution transmission electronic microscopy (TEM; Hitachi, HD-2700). More details on the physicochemical studies are reported elsewhere [41].

Electrodes composed of the materials described in Table 1 were prepared by using slurries with a mass ratio of 80:15:5, corresponding to active material varying between 1.6 g and 1.7 g, commercial conductive carbon, and polyvinylidene fluoride (PVDF), respectively. All the constituents of the slurry were dissolved in N-methyl-2-pyrrolidone (NMP). The final slurry was applied onto conductive carbon paper (Toray, Alfa Aesar, Haverhill, MA, USA) that worked as current collector and was dried at 50 °C for 24 h in an electric oven.

A Gamry Interface 1000 was employed for the electrochemical assessments that were performed in 1 M Na_2SO_4 and 1 M KOH electrolytes. A conventional electrochemical cell using three electrodes was adopted. The coated carbon was the working electrode, platinum foil (2.5 cm × 2.5 cm) served as the counter electrode, and a saturated calomel electrode (SCE) was adopted as reference. Cyclic voltammetry (CV) tests were performed at scan rates varying from 10 mV·s^{-1} to 400 mV·s^{-1}. Charge–discharge (GCD) curves were obtained in galvanostatic mode, and the applied current densities ranged from 0.4 to 10 A·g^{-1}.

Equation (1) was used to calculate the gravimetric capacitance C_s (F·g^{-1}) [3]:

$$C_s = \frac{i * \Delta t}{m * \Delta V} \tag{1}$$

where i is the current applied to the working electrode (A), Δt is the duration of discharge (s), m is the mass of the electroactive material (g), and ΔV is the potential window (V). The coulombic efficiency η was obtained using Equation (2) [42]:

$$\eta = \frac{t_d}{t_c} \times 100 \tag{2}$$

where t_d and t_c are, respectively, the durations (s) of discharge and charge.

The energy (E_d) and power (P_d) densities of a symmetric cell assembled with the prepared electrodes were computed using Equations (3) and (4), respectively [43]:

$$E_d = \frac{1}{2} * C_{cell} * \Delta V^2 \tag{3}$$

$$P_d = \frac{E_d}{t_d} \tag{4}$$

where C_{cell} is the cell-specific capacitance, ΔV is the cell working potential window, and t_d is the discharge time assessed at each current density from the galvanostatic charge–discharge tests.

Cycling stability was determined under 10 A·g^{-1} for 10,000 cycles in an uninterrupted galvanostatic charge–discharge test in the full potential window.

Electrochemical impedance spectroscopy (EIS) was also used to extract additional information about the electrochemical response of the dual-doped graphene material. The root mean square perturbation had an amplitude of 10 mV, and the spectra were taken in a frequency range of 0.01 to 10^5 Hz.

3. Results and Discussion

3.1. Physico-Chemical Results

The TEM images (Figure 1) indicate the morphology for S_3N_3_GF (a, b), while those for the other nanocomposites were reported in a previous work [40] and therefore are not repeated here. According to the micrographs, for the S_3N_3_GF precursor, we inferred that the materials were composed of wrinkled graphene sheets. Similar results were previously reported for other S, N-doped materials [40,41].
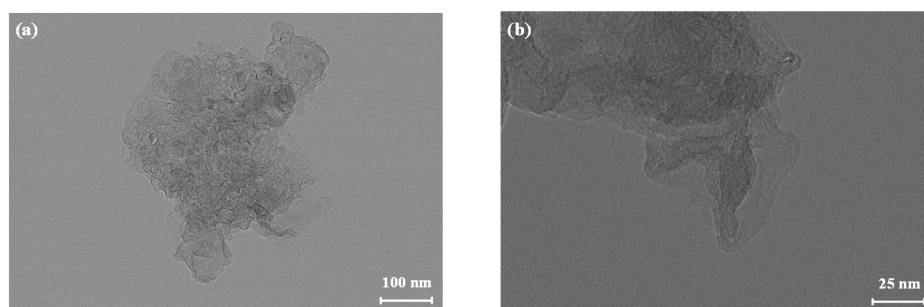
Figure 1. Representative TEM micrographs of S_3N_3‒GF (**a**,**b**).

The results obtained by Raman spectroscopy for the different precursors are depicted in Figure 2. All the spectra evidence the presence of the D, G, and 2D bands at 1342, 1564, and ~2680 cm^{-1}, respectively. The G band is related to the sp^2 configuration of carbon, and the D band is due to the existing defects in the graphene lattice [44]. The use of different N, S-containing compounds did not seem to affect the results of the different precursors, as all bands had the same positions and similar D/G intensity ratios, with values ranging between 0.51 and 0.56.
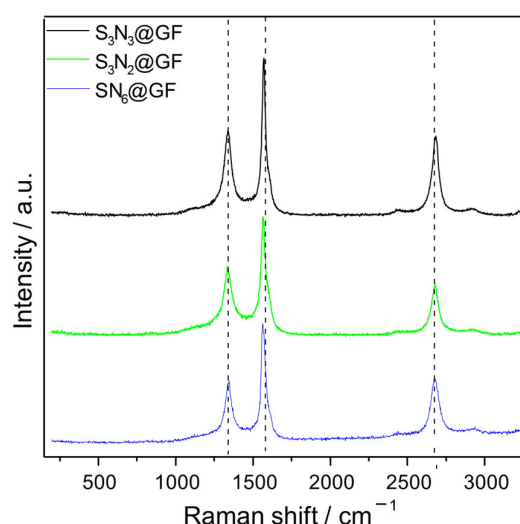

Figure 2. Raman spectra of S_3N_3‒GF (black), S_3N_2‒GF (green), and SN_6‒GF (blue).

The surface composition of all doped materials was studied by XPS, and the atomic percentages of the elements are displayed in Tables 2 and 3. O 1s photoionization is associated with the intrinsic concentration of oxygen functional groups such as C−O (phenol, epoxy, and hydroxyl), C=O (ketones, quinones, and aldehydes), and O−C=O (carboxylic acids and esters) that, according to the literature, can be present in bare graphene [39,45]. Farivar et al. [46] found an atomic concentration of 2.4% for graphene, while Limani et al. observed a concentration of approximately 4.1% [47]. The S 2p content was always lower than the N 1s content for all the materials tested. Yang et al. [48] claimed that the concentration of S is generally lower than that of N, even when the materials are subjected to high temperatures of around 500–900 °C, a route usually used to enhance thiophene-like doping onto graphene materials. However, it is likely that the low contents of sulfur in the graphene network were influenced by the high calcination temperature, which can partially remove sulfur particles [49]. Wu et al. [50] reported similar ratios of N and S and changes in S content at higher proportions of methionine (the precursor material). Relative Regarding oxygen, the highest content in the SN_6 material could be associated with the stability of O_2 on the preferential position in the N-quaternary structure among other nitrogen sites onto the graphene lattice [51].

Table 2. XPS atomic percentages for all prepared materials.

Sample	Atomic Percentage [a]				Atomic Ratio				
	C 1s	O 1s	N 1s	S 2p	$\frac{N+S}{C}$	$\frac{N+S}{C}$	$\frac{N}{C}$	$\frac{S}{C}$	$\frac{N}{S}$
S_3N_3_GF	96.7	1.8	1.2	0.3	1.55	1.55	1.24	0.31	4
S_3N_2_GF	97.4	1.1	1.3	0.2	1.54	1.54	1.33	0.21	6.5
SN_6_GF	93.9	3.2	2.6	0.3	3.08	3.08	2.77	0.31	8.7

[a] Values were calculated form the areas of the fitted peaks in the respective photoionization.

Table 3. Relative atomic percentages of nitrogen in the N1s photoionization.

Material	% N		
	398.1–398.6 eV (Pyridinic N)	399.3–400.1 eV (Pyrrolic N)	400.4–402.2 eV (Quaternary N)
S_3N_3_GF (25:75)	67.3	25.8	6.9
S_3N_2_GF (25:75)	63.6	23.1	13.3
SN_6_GF (25:75)	59.8	22.6	17.6

The C photoionizations (Figure 3a–c) were deconvoluted into seven peaks: the most intense one was observed at 284.6 eV and correlated to sp^2 C, which is typical of graphene structures; the peak at 285.2 eV corresponded to the sp^3 C hybridization; the peak at 285.9 eV could be ascribed to C-N; the one at 286.9 eV to the C in C-O-C; the peak at 288.2 eV likely resulted from the presence of C=O; at 289.3 eV, there was a possible contribution from O-C=O. At higher binding energies, 291.0 eV, there was a contribution assigned to $\pi - \pi^*$ transitions. Moreover, there was also participation of the C-S moieties; however, the binding energies in the 285.2–287 eV range were overlapped by the peaks at 285.2, 285.9, and 286.9 eV, implying the accuracy of the deconvolution [52].

The O 1s high-resolution photoionization of all S, N-doped materials (Figure 3d–f) was fitted with two peaks: one at ≈531.5 eV, correlated with O in two groups, i.e., C=O and COOH; and the other at ≈533.1 eV, belonging to oxygen in C-OH groups [48]. The N 1s photoionization (Figure 3g–i) was linked to the following peaks: at 398.1–398.6 eV, attributed to pyridinic-N; at 399.3–400.1 eV, assigned to pyrrolic-N (both peaks possessed a π-conjugated configuration and a pair of p electrons); at 400.4–402.2 eV, attributed to graphitic N. In this case, N atoms behaved as substitutes for C atoms [53,54]. Table 3 shows the relative atomic percentages of the different nitrogen contributions. The corresponding amount of N functionalities increased in the following manner: quaternary N < pyrrolic N < pyridinic N. Additionally, the amounts of pyridinic and pyrrolic N decreased in the sequence of S_3N_3, S_3N_2, and SN_6, while the quaternary N increased (6.9% to 17.6%). In general, high temperatures can decrease the concentration of dopant atoms. However, the current findings showed that graphitic species were enhanced at 800 °C during the calcination and permitted the formation of thermostable graphitic and pyridinic N structures [55], as displayed in Table 3. This suggests that higher N:S ratios in the precursor favor the development of substitutional N functionalities in doped graphene materials.

S 2p photoionization is depicted in Figure 3j–l. The spectra for the S, N-doped presented peaks at ≈164.0 eV ($2p_{3/2}$) and 165.1 eV ($2p_{1/2}$), ascribed to C-S-C covalent bonds; and peaks at ≈165.5 eV ($2p_{3/2}$) and 166.6 eV ($2p_{1/2}$), belonging to C-SH; and two others in the ranges of 167.6–168.1 eV and 169.2–170.4 eV, related to sulfur oxidation (-C-SOx-C, x = 2, 3).
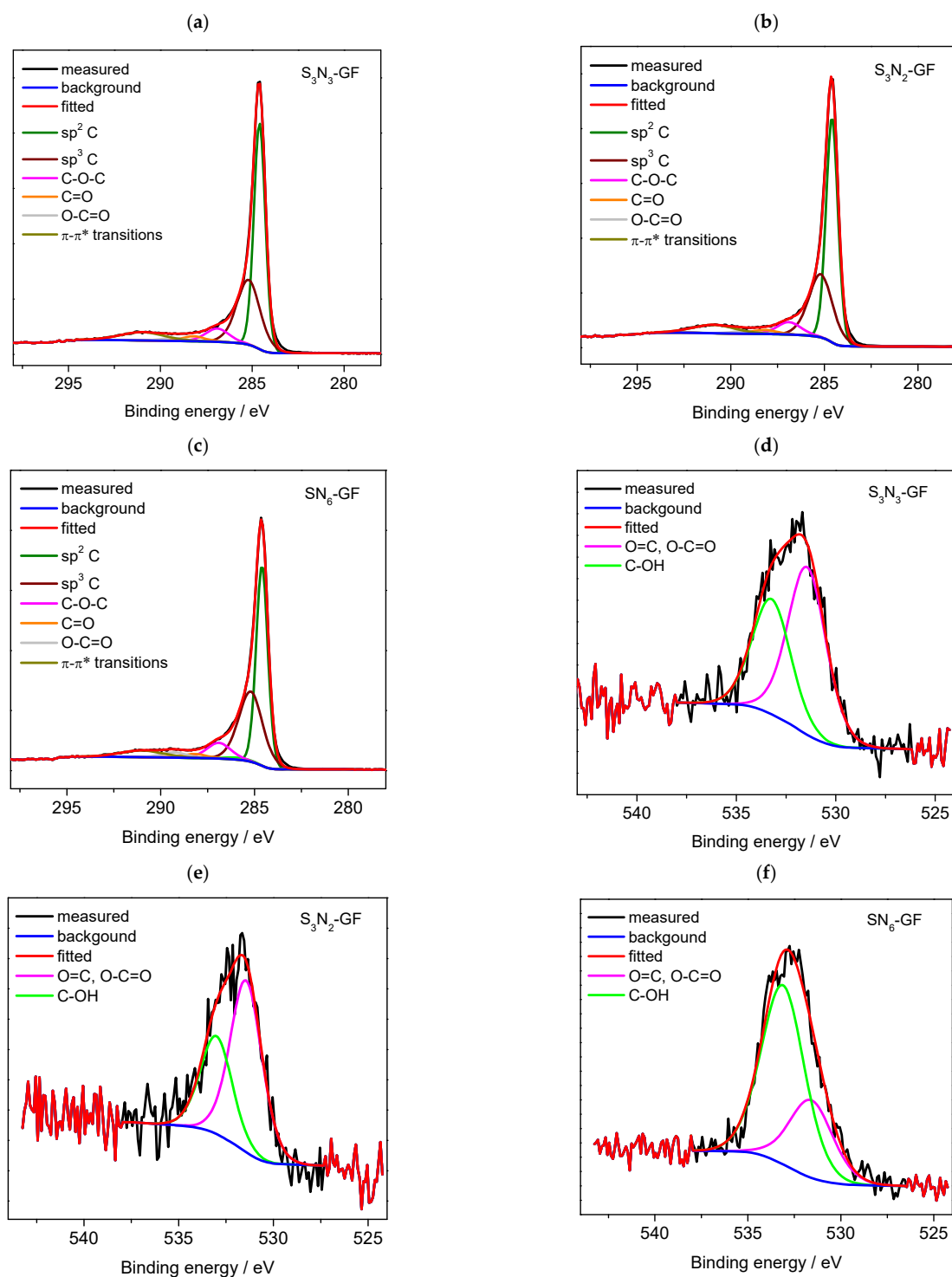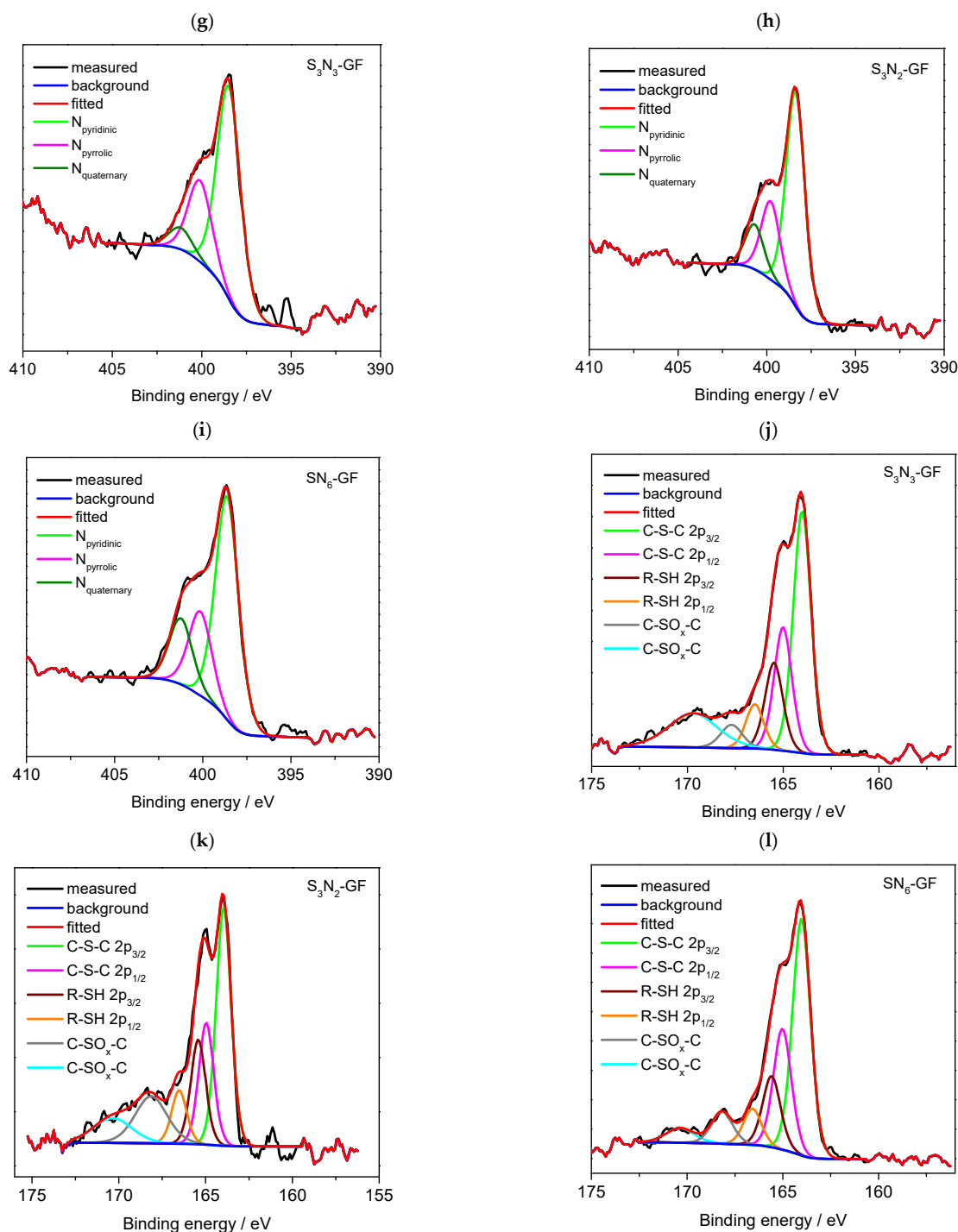
Figure 3. *Cont.*

Figure 3. Deconvolutions of: (**a**–**c**) C1s photoionization; (**d**–**f**) O1s photoionization; (**g**–**i**) N1s photoionization; (**j**–**l**) S2p photoionization.

As seen in Table 2, the contents of S and the S/C ratio were nearly independent of the precursors used. However, the N content significantly increased when SN_6 was used. This increase was also clear when analyzing the N/C atomic ratios and the N/S atomic ratios, which more than doubled compared with when SN_6 was used. This variation suggests that using N as the doping atom elevates the efficiency of quaternary N contribution in the precursor (Table 3).

3.2. Electrochemical Results

The electrochemical response of the electroactive materials was evaluated in 1 M Na_2SO_4 and 1 M KOH. The specific capacitance values obtained for the different electrodes are depicted in Tables 4 and 5, respectively; a comparison of their electrochemical performance is shown in Figures 4 and 5, respectively.

Table 4. Summary of specific capacitance values obtained for the different co-doped materials prepared in this study at different applied specific currents in 1 M Na_2SO_4.

Material/Applied at Specific Current Density ($A \cdot g^{-1}$)	Specific Capacitance ($F \cdot g^{-1}$)					
	1	2	4	6	8	10
SN_6_GF	48.4	46.9	45.5	44.5	43.8	42.8
S_3N_2_GF	41.9	40.9	39.2	37.8	36.5	35.3
S_3N_3_GF	23.6	23.2	22.7	22.3	21.8	21.3

Table 5. Summary of specific capacitance values obtained for the different co-doped materials prepared in this study at different applied specific currents in 1 M KOH.

Material/Applied at Specific Current Density ($A \cdot g^{-1}$)	Specific Capacitance ($F \cdot g^{-1}$)					
	1	2	4	6	8	10
SN_6_GF	21.4	20.1	18.5	16.9	15.4	14.4
S_3N_2_GF	13.8	12.8	10.9	9.3	7.1	4.4
S_3N_3_GF	18.3	17.4	15.6	14.1	11.9	9.7

Figure 4a illustrates the cyclic voltammetry (CV) plots at a scan rate of 50 $mV \cdot s^{-1}$ in 1 M Na_2SO_4, and Figure 5a shows the voltammograms obtained in 1 M KOH. The quasirectangular shapes obtained in both electrolytes indicated an almost ideal and highly reversible charge storage process, with contributions from the double layer and pseudocapacitance, because weak redox humps were noticed in the presence of the heteroatom groups [56,57]. Additionally, for both electrolytes, the area under the CV for SN_6_GF (25:75) was larger than for the other co-doped materials and presented a larger potential window, ranging from −0.10 to 1.0 V in 1 M Na_2SO_4 and −0.15 to 0.4 V in 1 M KOH. Considering the charge–discharge results obtained for 1 $A \cdot g^{-1}$ in 1 M Na_2SO_4 (Figure 4b), the capacitance of the different materials reached a maximum of 48 $F \cdot g^{-1}$, 41.9 $F \cdot g^{-1}$, and 25.74 $F \cdot g^{-1}$ for SN_6_GF, S_3N_2_GF, and S_3N_3_GF, respectively. This shows that the precursor has an important role in electrode capacitance, which is enhanced in the presence of an increased N/S ratio with a larger contribution of quaternary nitrogen groups. In 1 M KOH (Figure 5b and Table 5), the specific capacitance of the materials was inferior in comparison with that of the neutral aqueous electrolyte: 21.4 $F \cdot g^{-1}$ for SN_6_GF, and 13.8 $F \cdot g^{-1}$ and 18.3 $F \cdot g^{-1}$ for S_3N_2_GF and S_3N_3_GF, respectively. All materials presented a coulombic efficiency (η) of ca. 100% in both electrolytes. It is worth noting that in addition to the higher specific capacitance in the neutral electrolyte, the potential window was also significantly extended compared with that of the alkaline electrolyte, even though the ionic conductivity of Na^+ ion (50.1 S cm^2 mol^{-1}) is inferior to that of K^+ (73.5 S cm^2 mol^{-1}). However, the electrochemical performance, namely, specific capacitance, rate capability, and cycling, are not affected by the ionic conductivity of ions: other parameters also play a vital role, such as the concentration, the size of the solvated ions, and pH conditions [58,59]. The performance of carbon-based electrodes is also affected by the morphologies and porous architectures of the material and the surface areas that expose more active sites for ion adsorption, as well as by the interaction between the surface functionalities of the electrode material and the nature of the electrolyte [15,59]. Tao et al. [60] also reported higher potential windows for N-doped graphene material in neutral sulfate-based electrolytes (2M $MgSO_4$ (1.8 V),

4M $MnSO_4$ (1.9 V), 1.3M $CoSO_4$ (1.5 V), 1.7M $NiSO_4$ (1.5 V), and 1 M $Al_2(SO_4)_3$ (1.5 V)). As reported by these authors, SO_4^{-2} inorganic anions have a solvation energy of around 108 kJ mol^{-1} per SO_4^{-2}-H_2O bonding unit, which represents more energy to break the sulfate-and-water interactions, permitting safe operation in an extended potential range without compromising the electrochemical performance via water decomposition. The cation sizes in KOH (K^+, 1.33 Å) and Na_2SO_4 (Na^+, 0.95 Å) may also contribute to the differences in specific capacitance. Quicker ion transportation is assisted by well-matched electrode pore size and ion size, which permit the facile access of the ions to the electrode surface [61]. Therefore, the electrochemical efficiency of doped graphene in 1 M Na_2SO_4 electrolyte might be influenced by the smaller size of Na^+.
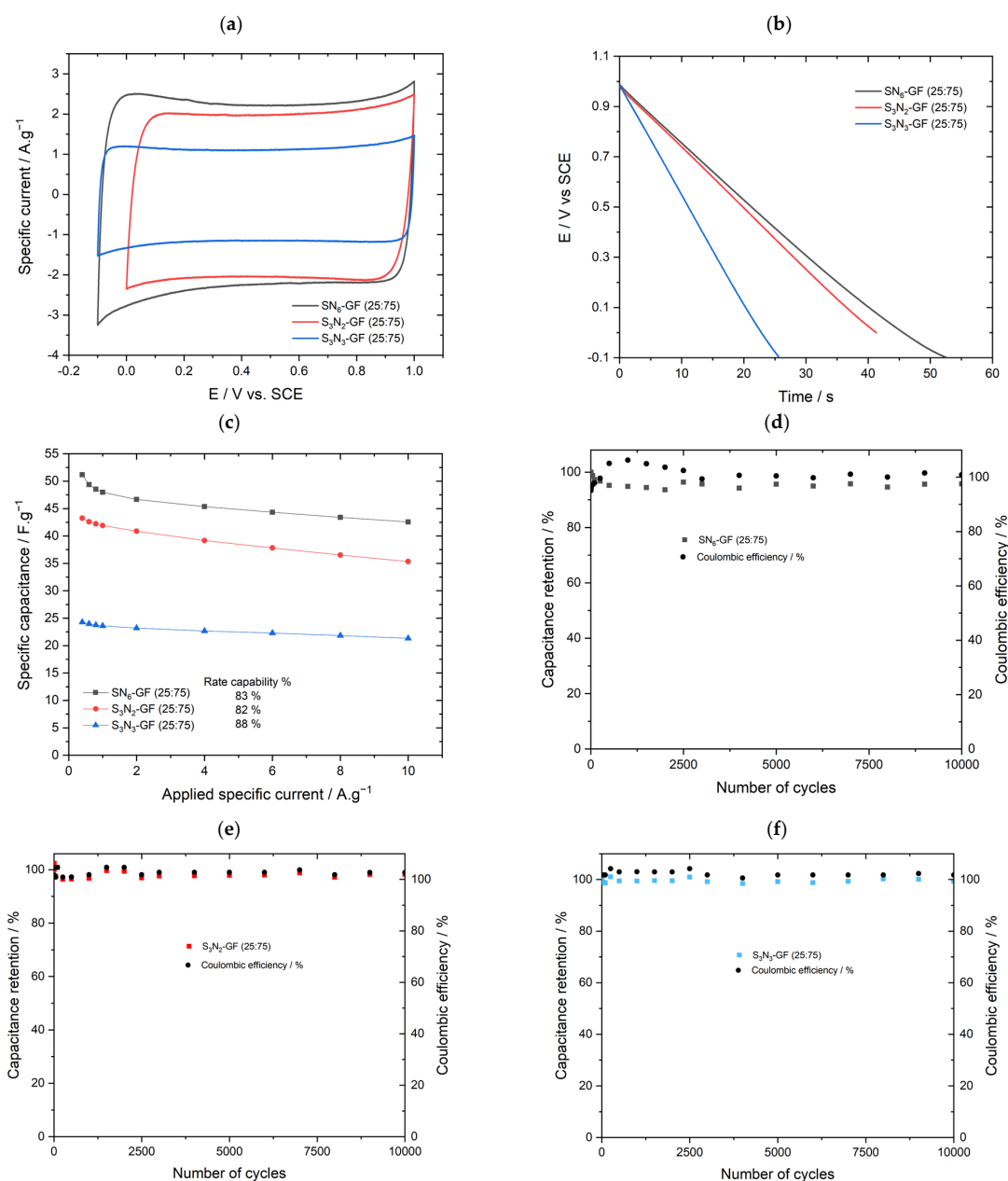

Figure 4. Electrochemical results for different dopants and different dopant ratios in 1 M Na_2SO_4 electrolyte, for SN_6_GF (25:75), S_3N_2_GF (25:75), and S_3N_3_GF (25:75): (**a**) cyclic voltammetry at 50 mV·s^{-1}; (**b**) discharge curves at 1.0 A·g^{-1}; (**c**) specific capacitance at specific current from 0.4 A·g^{-1} to 10.0 A·g^{-1}; and capacitance retention after 10,000 cycles of continuous charge–discharge at 10.0 A·g^{-1} for (**d**) SN_6_GF (25:75), (**e**) S_3N_2_GF (25:75) and (**f**) S_3N_3_GF (25:75).
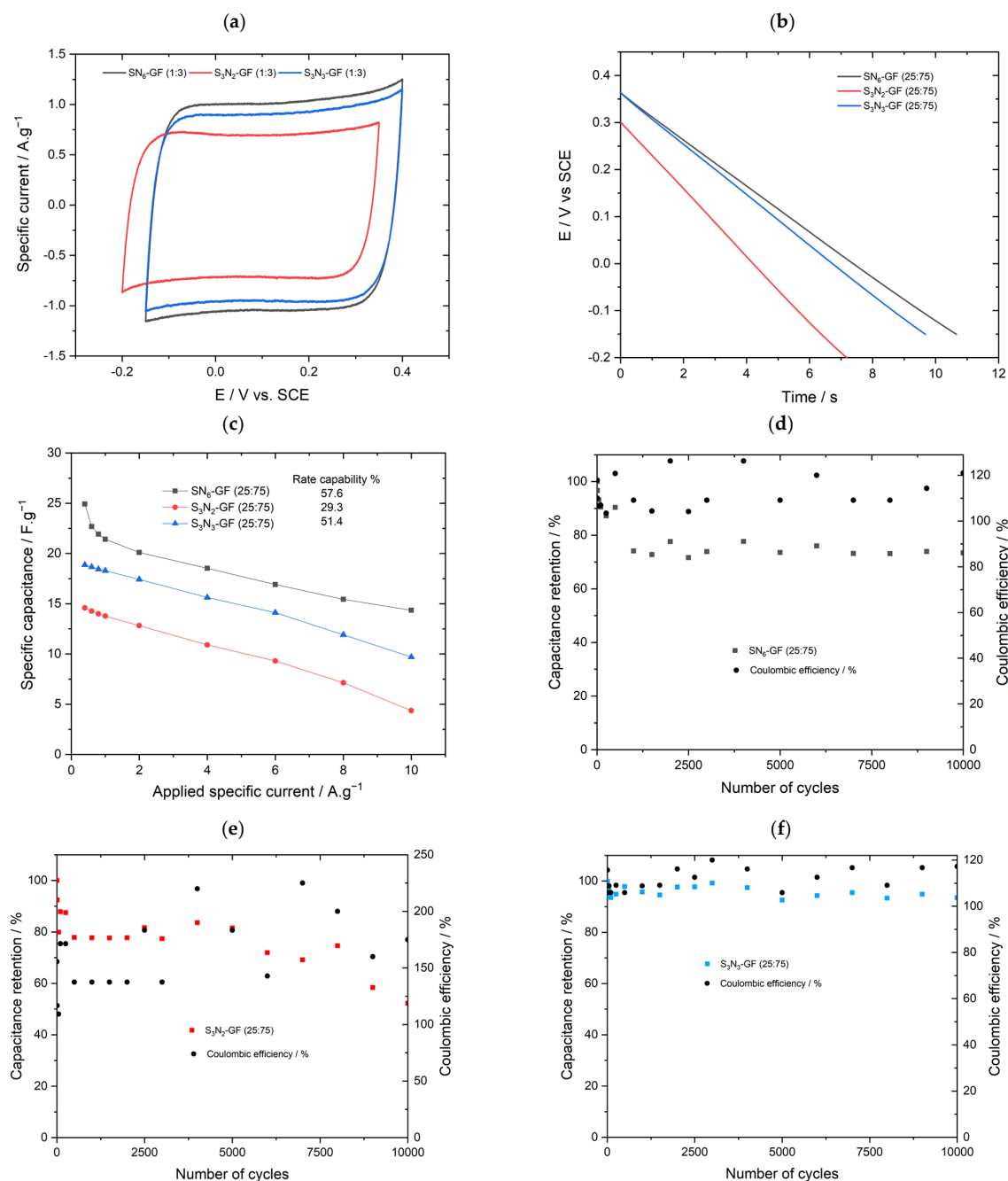
Figure 5. Electrochemical results for different dopants and different dopant ratios in 1 M KOH electrolyte for SN_6–GF (25:75), S_3N_2–GF (25:75), and S_3N_3–GF (25:75): (**a**) cyclic voltammetry at 50 mV·s^{-1}; (**b**) discharge curves at 1.0 A·g^{-1}; (**c**) specific capacitance at different applied specific current from 0.4 A·g^{-1} to 10.0 A·g^{-1}; and capacitance retention after 10,000 cycles of charge–discharge at 10.0 A·g^{-1} for (**d**) SN_6–GF (25:75), (**e**) S_3N_2–GF (25:75), and (**f**) S_3N_3–GF (25:75).

As depicted in Figures 4c and 5c, the specific capacitance linearly decreased with the applied specific currents; larger currents promote faster reactions, hampering diffusion-controlled processes [57], which may affect the double-layer formation. Adding an appropriate content of dopants into graphene contributes to increasing the specific capacitance, due to the enhanced double layer and additional pseudocapacitance performance [62]. Figure 4c evidences the rate capabilities above 80% for all the electrode materials; S_3N_3 showed the highest rate capability (88%) in neutral media. In KOH electrolytes, the rate capability was more sensitive to the type of electrode, with S_3N_2 displaying the poorest

rate. Both S_3N_3 and SN_6 display similar values that, however, were significantly below those observed in neutral media. Moreover, these results agree with those previously reported in literature. For example, Xing et al. [63] studied N,S co-doped graphene using thiocarbohydrazide (SN_4) as the dopant in 6M KOH. The electrochemical measurements revealed a rate capability of 59.4% to a maximum of 72.3% at 10 A·g^{-1}.

The capacitance retention of all the electrode materials was determined after 10,000 cycles of successive charge–discharge cycles at 10 A·g^{-1} (Figures 4d–f and 5d–f). In neutral media, all materials retained above 90% of their initial capacitance: SN_6_GF (95.8%), S_3N_2_GF (98.2%), and S_3N_3_GF (99.4%). Conversely, in 1 M KOH (Figure 5f), only S_3N_3_GF presented a higher capacitance retention of around 93.5%, against 73.3% and 52.2% for SN_6_GF and S_3N_2_GF, respectively. As stated above, the S_3N_3 precursor 1,3,5-triazine-2,4,6-trithiol has a relative atomic percentage (67.3%) of pyridinic N that is more pronounced than that of other dopants, as depicted in Table 3; this might positively affect the stability of the electrode. This advantage was observed by Balaji et al. [58], who reported that pyridinic N permits enhanced interactions with electrolyte ions. Thus, the higher concentration of pyrrolic N (25.8%) in S_3N_3 compared with that in the other materials contributed to the increased electrochemical stability of the material. The excellent cyclability performance of the doped materials in neutral media could be also associated with the pore structure, good electrode–electrolyte interactions, and the double-layer nature of the charge–storage mechanism [64]. As seen in Table 2, higher atomic percentages of the dopants (-S plus -N) were measured for SN_6_GF, which revealed the highest capacitance and overall excellent electrochemical stability in 1 M Na_2SO_4. This was probably due to the more stable atomic bonds enhancing the charge-transfer rate [65]. In KOH, the material seemed more prone to fading during current and cycling, leading to poorer electrochemical stability.

The results discussed above indicate that the N,S-doped GF (SN_6_GF), obtained from 4-amino-3-hydrazino-5-mercapto-1,2,4-triazole in a 25:75 ratio yielded the most interesting results in 1 M Na_2SO_4 (Table 4), likely caused by the efficient interconnection of N and S functional groups with the C atoms of bare graphene [66]. The literature shows that doping generally enhances the electrochemical activity and electron transfer kinetics [12], without compromising the power density or long-term cyclability [67]. However, there is no extensive literature on the influence of the precursor on the electrochemical reaction of the electrodes [68]. The results also evidence that the original precursor composition has an important role in both electrode specific capacitance and stability. As seen in Table 2, SN_6 introduces a higher content of N as a dopant, contributing to an increase in the specific capacitance. The electronegativity derived from nitrogen produces dipoles on the surface of the electrode that may facilitate the access of charged species to the material surface [55,56]. The elevated atomic ratio of oxygen content was also stimulated by mechanosynthesis, as observed with SN_6_GF inducing superior specific capacitance among the considered materials. Moreover, a high oxygen content benefits the wettability and mobility of ions to access the pores [69].

A more detailed electrochemical analysis of SN_6_GF (25:75) in 1 M Na_2SO_4 is shown in Figure 6 in the −0.1 V to 1.0 V vs. SCE potential range. Identical information for S_3N_3_GF (25:75) and S_3N_2_GF (25:75) can be found in Figures S1 and S2, respectively. For the SN_6 electrode, as the scan rate increased, the curves (Figure 6a) retained their nearly rectangular shape even at the highest scan rate of 400 mV·s^{-1}. This result agrees with those observed by Quin et al. [66], who investigated co-doping using thiourea and verified quasirectangular CVs up to 200 mV·s^{-1}. Additionally, the SN_6 electrode showed quasisymmetric triangular curves (Figure 6b), resulting in high coulombic efficiency [57]. Figure S2 for 1 M Na_2SO_4 and Figures S3–S5 for 1 M KOH demonstrate that this electrode started to deviate from the rectangle-like shape at scan rates above 200 mV·s^{-1}.

Further electrochemical information was obtained by assembling a two-electrode symmetric cell using the best co-doped electrode material, i.e., a SN_6_GF//SN_6_GF cell. Na_2SO_4 was used as it provides a wider potential window, in agreement with the literature [70]. As depicted in Figure 6c, the CV curves obtained at scan rates from 10 mV·s^{-1} to

400 mV·s^{-1} showed a quasirectangular shape up to 150 mV·s^{-1} and a potential window between 0 V to 1.5 V. Moreover, symmetrical triangular shapes in the GCD curves (Figure 6d) were observed at different current densities from 0.4 A·g^{-1} to 10 A·g^{-1} indicating the capacitive response of the cell. The specific capacitance (Figure 6e) of the $SN_6\text{–GF}//SN_6\text{–GF}$ at 1.0 A·g^{-1} was 17.4 F·g^{-1}, and the rate capability was 35.6%. Furthermore, the capacitance retention of the cell was around 66.7% after 10,000 successive charge/discharge cycles at 10 A·g^{-1} (Figure 6f). These results are consistent with a reversible double-layer charge storage mechanism [71]. Notably, this cell reached a higher potential window of 1.5 V, which is reported for the first time for this precursor. The power density and energy density values were estimated and are depicted in the Ragone plot in Figure 6g, which reached 717.7 W·kg^{-1} and 4.98 W·h·kg^{-1} at 1 A·g^{-1}, respectively.

Figure 6. *Cont.*

(g)
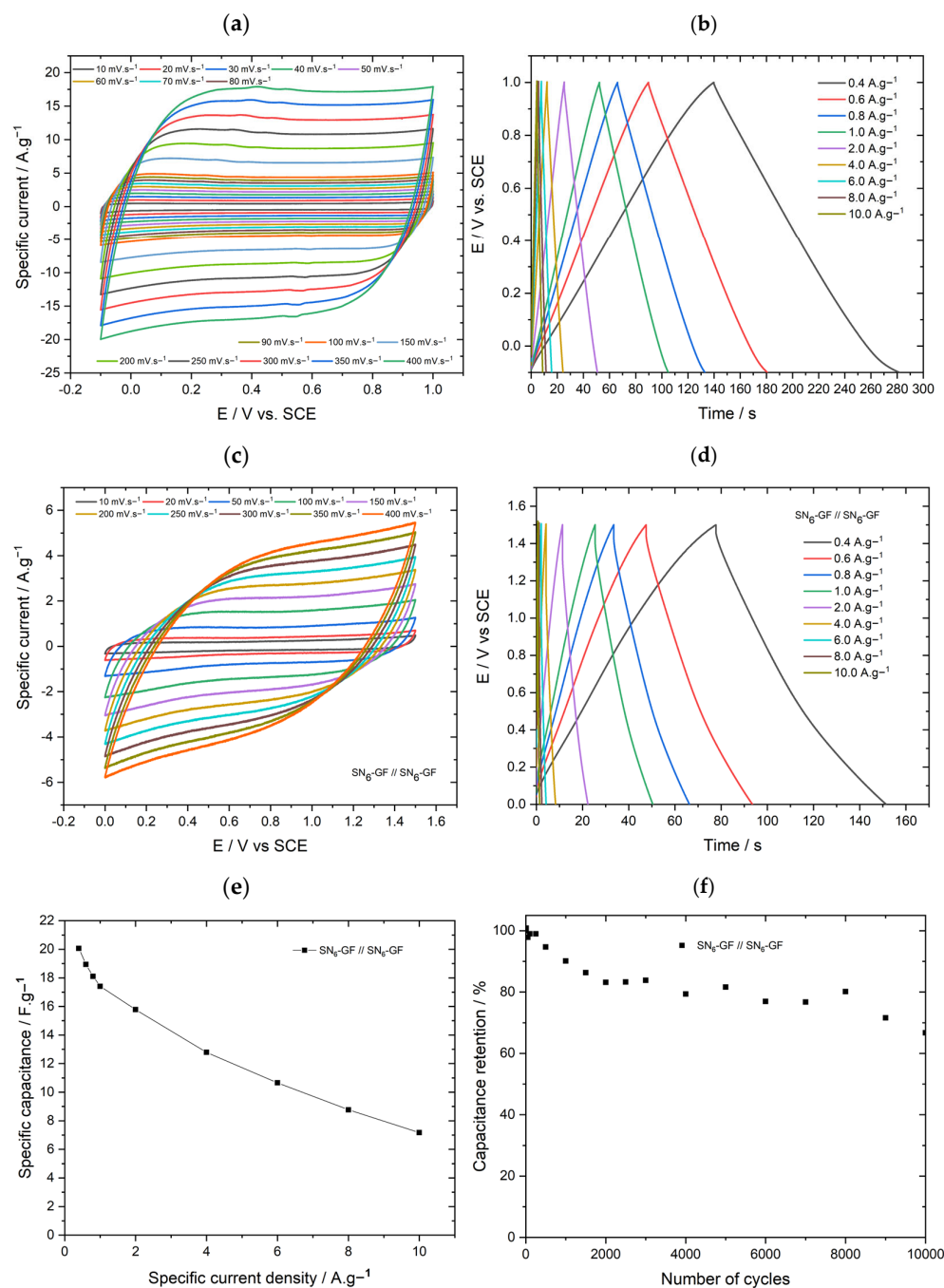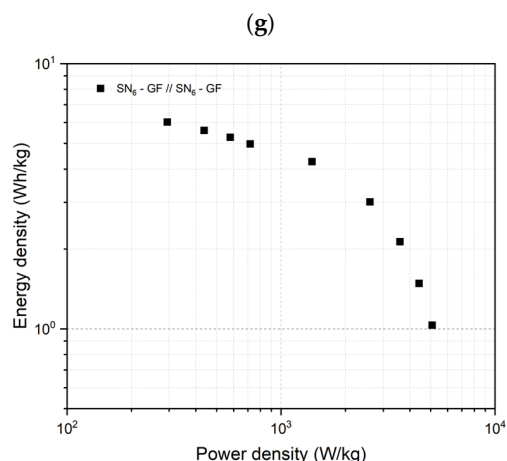
Figure 6. SN_6_GF (25:75): (**a**) cyclic voltammetry at scan rates ranging from $10\,mV\cdot s^{-1}$ to $400\,mV\cdot s^{-1}$. Potential window from -0.10 V to 1.0 V vs. SCE (1 M Na_2SO_4) electrolytes; (**b**) galvanostatic charge−discharge at applied specific currents from 0.4 to 10 $A\cdot g^{-1}$ in 1 M Na_2SO_4 electrolytes. Electrochemical performance of the $SN_6\_GF//SN_6\_GF$ symmetric cell in 1 M Na_2SO_4 electrolyte: (**c**) CV curves at scan rates from $10\,mV\cdot s^{-1}$ to $400\,mV\cdot s^{-1}$; (**d**) galvanostatic charge−discharge at applied specific currents of 0.4 to 10 $A\cdot g^{-1}$; (**e**) specific capacitance at applied specific current from $0.4\,A\cdot g^{-1}$ to $10.0\,A\cdot g^{-1}$; (**f**) capacitance retention after 10,000 cycles of continuous charge−discharge at 10.0 $A\cdot g^{-1}$; (**g**) Ragone plots of $SN_6\_GF//SN_6\_GF$ symmetric device.

Electrochemical impedance spectroscopy (EIS) studies were performed in 1 M Na_2SO_4 to further assess the electrochemical response of the S/N co-doped graphene. EIS provides data about the equivalent series resistance (ESR), which is used to understand a system's resistance, including the current collector, electrolyte, and active material [58]. Li et al. claimed that doping graphene with heteroatoms, namely S and N, may change the layered structure of a graphene lattice due to the formation of defects arising from replaced carbon atoms. Moreover, this doping enhances the capacitance and the charge-transfer processes in the material [59].

The EIS results for the SN_6_GF are depicted in Figure 7a–d. The electrodes presented phase angle values close to $-90°$ and a marked capacitive response in the low-frequency range, which evidenced the quasi-ideal supercapacitive behavior of this material, as expected for carbon-based materials. This is a consequence of the enhanced electron transport that is associated with low series resistance and easier charge transfer. Additionally, SN_6_GF electrodes showed stable resistance values on cycling (Rs), 2.78 Ω (cycle 0) and 2.82 Ω (cycle 10,000); the slightly enhanced real capacitance over cycling demonstrated the high electroconductivity of this material [60]. There was a very minimal reduction in the phase angle after 10,000 cycles, which could likely be attributed to minimal irreversible oxidation phenomena at the electrode surface [61]. Moreover, the small or depressed semicircle in the Nyquist plot (Figure 7c) showed a low charge-transfer resistance for SN_6_GF, even after the cycling stability test. This was a consequence of the enhanced electron transport associated with the low series resistance and easier charge transfer of the materials.
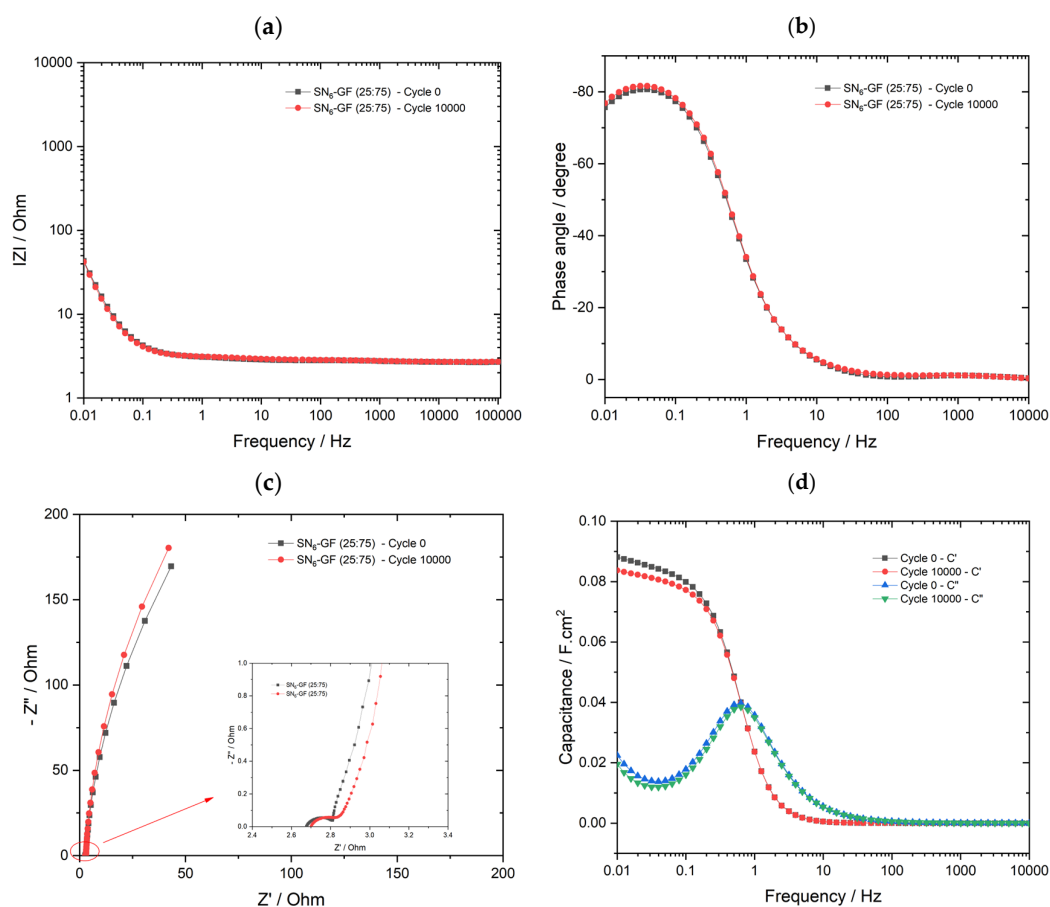
Figure 7. Electrochemical impedance spectroscopy results for co-doped graphene sample in 1 M Na$_2$SO$_4$ electrolyte, SN$_{6-}$GF (25:75): (**a**) magnitude Bode plots; (**b**) Bode plots vs. phase angle; (**c**) Nyquist plot; and (**d**) complex capacitance analysis.

The imaginary capacitance is related to the energy dissipation due to the dielectric loss of electrolyte ions due to the influence of frequency on either their movement or rotation. The progress of the imaginary capacitance accounts for a relaxation time (1/f at the maximum) of approximately 1 s [62,63]. This is the so-called factor of merit, which is also used to characterize electrode performance. It corresponds to the time necessary to discharge the electrode with an efficiency above 50% [64,65]. The relaxation time for SN$_{6-}$GF was 0.25 s, which is slightly lower in comparison with those of other investigated co-doped materials. A short relaxation time indicates an elevated ion transport rate between the electrode and electrolyte interfaces [66]. In Kumar et al. [67], the relaxation time was 0.28 s for multiheteroatom doped graphene: nitrogen, phosphorous, and fluorine (NPFG), in 6M KOH. Otherwise, in other forms of N-S doped carbons proposed by Zhou et al. [68], the time constant corresponded to 0.33 s in 1 M KOH, which is comparable to that of the SN$_{6-}$GF electrode, ensuring high electrochemical performance for the 4-amino-3-hydrazino-5-mercapto-1,2,4-triazole precursor.

4. Conclusions

S,N co-doped graphene electrode materials for electrochemical double-layer capacitors were successfully prepared by ball milling using different S and N precursors. The concentration of S in the doped graphene was independent of the precursor concentration, while the amount of nitrogen and the relative concentrations of quaternary, pyridinic, and pyrrolic N functionalities were dependent on the chemical nature of the precursor. Among the investigated precursors, SN$_6$ (4-amino-3-hydrazino-5-mercapto-1,2,4-triazole) had the highest content of quaternary N groups, the highest specific capacitance values, and ex-

cellent stability in neutral electrolytes. The specific capacitance attained was 48 F·g^{-1} at 1.0 A·g^{-1}, and the capacitance retention was above 90% after 10,000 cycles in 1 M Na$_2$SO$_4$. All the tested precursors resulted in electrodes that displayed much better electrochemical performance in Na$_2$SO$_4$ than KOH, which induced a more marked performance loss either in terms of current density or cycling for all the electrodes. In 1 M KOH, the SN$_6$ electrode displayed the highest rate capability (57.6%) and the highest specific capacitance of 21.4 F·g^{-1} at 1 A·g^{-1} in comparison with those of the other materials tested in the same electrolyte. Interestingly, the electrodes prepared using S$_3$N$_3$ (1,3,5-triazine-2,4,6-trithiol) as the precursor for N and S achieved a higher rate capability (88% of its initial specific capacitance at 10 A·g^{-1}) in 1 M Na$_2$SO$_4$ and the uppermost capacitance retention at 10 A·g^{-1} in both electrolytes. Overall, the nature of the N and S precursors had a strong influence on the electrochemical response of the electrode in different electrolytes.

Supplementary Materials: The following supporting information can be downloaded at: https://www.mdpi.com/article/10.3390/batteries9030168/s1. Figure S1. S$_3$N$_3$_GF (25:75): (a) cyclc voltammetry at different scan rates ranging from 10 mV.s^{-1} to 400 mV.s^{-1}. Potential window from −0.15 V to 1.0 V vs. SCE (1 M Na$_2$SO$_4$) electrolytes; (b) galvanostatic charge–discharge at different applied specific currents from 0.4 to 10 A.g^{-1} in 1 M Na$_2$SO$_4$ electrolyte; Figure S2. S$_3$N$_2$_GF (25:75): (a) cyclic voltammetry at different scan rates ranging from 10 mV.s^{-1} to 400 mV.s^{-1}. Potential window from 0.0 V to 1.0 V vs. SCE in 1 M Na$_2$SO$_4$ electrolyte; (b) galvanostatic charge–discharge at different applied specific currents from 0.4 to 10 A.g^{-1} in 1 M Na$_2$SO$_4$ electrolytes; Figure S3. SN$_6$_GF (25:75): (a) cyclic voltammetry at different scan rates ranging from 10 mV.s^{-1} to 400 mV.s^{-1}. Potential window from −0.15 V to 0.4 V vs. SCE in 1 M KOH electrolyte; (b) galvanostatic charge–discharge at different applied specific currents from 0.4 to 10 A.g^{-1} in 1 M KOH electrolyte; Figure S4. S$_3$N$_3$_GF (25:75): (a) cyclic voltammetry at different scan rates ranging from 10 mV.s^{-1} to 400 mV.s^{-1}. Potential window from −0.15 V to 0.4 V vs. SCE in 1 M KOH electrolyte; (b) galvanostatic charge–discharge at different applied specific currents from 0.4 to 10 A.g^{-1} in 1 M KOH electrolyte; Figure S5. S$_3$N$_2$_GF (25:75): (a) cyclic voltammetry at different scan rates ranging from 10 mV.s^{-1} to 400 mV.s^{-1}. Potential window from −0.15 V to 0.4 V vs. SCE in 1 M KOH electrolyte; (b) galvanostatic charge–discharge at different applied specific currents from 0.4 to 10 A.g^{-1} in 1 M KOH electrolyte.

Author Contributions: Conceptualization, A.A.-M., T.M.S. and M.F.M.; methodology, D.M.F., A.A.-M., T.M.S. and M.F.M.; validation, T.M.S. and M.F.M.; investigation, R.B., D.M.F., A.A.-M., T.M.S. and M.F.M.; resources, D.M.F., A.A.-M., T.M.S. and M.F.M.; writing—original draft preparation, R.B., D.M.F., A.A.-M., T.M.S. and M.F.M.; writing—review and editing, R.B., D.M.F., A.A.-M., T.M.S. and M.F.M.; supervision, T.M.S. and M.F.M.; project administration, M.F.M.; funding acquisition, M.F.M. All authors have read and agreed to the published version of the manuscript.

Institutional Review Board Statement: Not applicable.

Informed Consent Statement: Not applicable.

Data Availability Statement: No new data were created or analyzed in this study. Data sharing is not applicable to this article.

Conflicts of Interest: The authors declare no conflict of interest.

References

1.　Dai, Z.; Ren, P.G.; Jin, Y.L.; Zhang, H.; Ren, F.; Zhang, Q. Nitrogen-sulphur Co-doped graphenes modified electrospun lignin/polyacrylonitrile-based carbon nanofiber as a high-performance supercapacitor. *J. Power Sources* **2019**, *437*, 226937. [CrossRef]

2.　Alcaraz, L.; Adán-Más, A.; Arévalo-Cid, P.; de Fatima Montemor, M.; López, F.A. Activated Carbons From Winemaking Biowastes for Electrochemical Double-Layer Capacitors. *Front. Chem.* **2020**, *8*, 686. [CrossRef] [PubMed]

3.　Almeida, M.M.; Más, A.A.; Silva, T.M.; Montemor, M.F. From manganese oxide to manganese sulphide: Synthesis and its effect on electrochemical energy storage performance. *Electrochim. Acta* **2021**, *389*, 138711. [CrossRef]

4.　Zhang, J.; Li, Y.; Han, M.; Xia, Q.; Chen, Q.; Chen, M. Constructing ultra-thin Ni-MOF@NiS$_2$ nanosheets arrays derived from metal organic frameworks for advanced all-solid-state asymmetric supercapacitor. *Mater. Res. Bull.* **2020**, *137*, 111186. [CrossRef]

5.　Chen, Y.; Sun, L.; Liu, Z.; Jiang, Y.; Zhuo, K. Synthesis of nitrogen/sulfur co-doped reduced graphene oxide aerogels for high-performance supercapacitors with ionic liquid electrolyte. *Mater. Chem. Phys.* **2019**, *238*, 121932. [CrossRef]

6.　Adan-Mas, A.; Alcaraz, L.; Arévalo-Cid, P.; López-Gómez, F.A.; Montemor, F. Coffee-derived activated carbon from second biowaste for supercapacitor applications. *Waste Manag.* **2021**, *120*, 280–289. [CrossRef]

7.　Xu, Y.; Lu, W.; Xu, G.; Chou, T.W. Structural supercapacitor composites: A review. *Compos. Sci. Technol.* **2021**, *204*, 108636. [CrossRef]

8.　Tang, X.; Zhang, B.; Lui, Y.H.; Hu, S. Ni-Mn bimetallic oxide nanosheets as high-performance electrode materials for asymmetric supercapacitors. *J. Energy Storage* **2019**, *25*, 100897. [CrossRef]

9.　Chen, X.; Chen, X.; Xu, X.; Yang, Z.; Liu, Z.; Zhang, L.; Xu, X.; Chen, Y.; Huang, S. Sulfur-doped porous reduced graphene oxide hollow nanosphere frameworks as metal-free electrocatalysts for oxygen reduction reaction and as supercapacitor electrode materials. *Nanoscale* **2014**, *6*, 13740–13747. [CrossRef]

10.　Li, J.; Zhang, G.; Fu, C.; Deng, L.; Sun, R.; Wong, C.P. Facile preparation of nitrogen/sulfur co-doped and hierarchical porous graphene hydrogel for high-performance electrochemical capacitor. *J. Power Sources* **2017**, *345*, 146–155. [CrossRef]

11.　Guo, M.; Balamurugan, J.; Li, X.; Kim, N.H.; Lee, J.H. Hierarchical 3D Cobalt-Doped Fe$_3$O$_4$ Nanospheres@NG Hybrid as an Advanced Anode Material for High-Performance Asymmetric Supercapacitors. *Small* **2017**, *13*, 1701275. [CrossRef]

12.　Zhang, J.; Zhou, J.; Wang, D.; Hou, L.; Gao, F. Nitrogen and sulfur codoped porous carbon microsphere: A high performance electrode in supercapacitor. *Electrochim. Acta* **2016**, *191*, 933–939. [CrossRef]

13.　Zhang, L.; Chen, H.; Lu, X.; Wang, Y.; Tan, L.; Sui, D.; Qi, W. Fabrication of N, S co-doped graphene aerogel for high-performance supercapacitors: π-conjugated planar molecules as efficient dopants and pillared agents. *Appl. Surf. Sci.* **2020**, *529*, 147022. [CrossRef]

14.　Zhou, Y.; Zeng, Y.; Xu, D.; Li, P.; Wang, H.-G.; Li, X.; Li, Y.; Wang, Y. Nitrogen and sulfur dual-doped graphene sheets as anode materials with superior cycling stability for lithium-ion batteries. *Electrochim. Acta* **2015**, *184*, 24–31. [CrossRef]

15.　Vlachova, J.; Tmejová, K.; Kopel, P.; Korabik, M.; Zitka, J.; Hynek, D.; Kynicky, J.; Adam, V.; Kizek, R. A 3D microfluidic chip for electrochemical detection of hydrolysed nucleic bases by a modified glassy carbon electrode. *Sensors* **2015**, *15*, 2438–2452. [CrossRef] [PubMed]

16.　Ma, L.; Liu, J.; Lv, S.; Zhou, Q.; Shen, X.; Mo, S.; Tong, H. Scalable one-step synthesis of N,S co-doped graphene-enhanced hierarchical porous carbon foam for high-performance solid-state supercapacitors. *J. Mater. Chem. A* **2019**, *7*, 7591–7603. [CrossRef]

17.　Upadhyay, K.K.; Bundaleska, N.; Abrashev, M.; Teodoro, O.; Fonseca, I.; de Ferro, A.M.; Silva, R.P.; Tatarova, E.; Montemor, M. Free-standing N-Graphene as conductive matrix for Ni(OH)2 based supercapacitive electrodes. *Electrochim. Acta* **2020**, *334*, 135592. [CrossRef]

18.　Ferrero, G.A.; Fuertes, A.B.; Sevilla, M. N-doped microporous carbon microspheres for high volumetric performance supercapacitors. *Electrochim. Acta* **2015**, *168*, 320–329. [CrossRef]

19.　Wang, L.J.; Zgierski, M.Z. Structures of Nitrogen-Rich Sulfides: SN 5 and SN 6. *J. Phys. Chem. A* **2004**, *108*, 4679–4684. [CrossRef]

20.　Jiang, Z.J.; Jiang, Z.; Chen, W. The role of holes in improving the performance of nitrogen-doped holey graphene as an active electrode material for supercapacitor and oxygen reduction reaction. *J. Power Sources* **2014**, *251*, 55–65. [CrossRef]

21.　Gopalsamy, K.; Balamurugan, J.; Thanh, T.D.; Kim, N.H.; Lee, J.H. Fabrication of nitrogen and sulfur co-doped graphene nanoribbons with porous architecture for high-performance supercapacitors. *Chem. Eng. J.* **2017**, *312*, 180–190. [CrossRef]

22.　Xu, X.; Zeng, H.; Han, D.; Qiao, K.; Xing, W.; Rood, M.J.; Yan, Z. Nitrogen and Sulfur Co-Doped Graphene Nanosheets to Improve Anode Materials for Sodium-Ion Batteries. *ACS Appl. Mater. Interfaces* **2018**, *10*, 37172–37180. [CrossRef] [PubMed]

23.　Shaikh, J.S.; Shaikh, N.S.; Kharade, R.; Beknalkar, S.A.; Patil, J.V.; Suryawanshi, M.P.; Kanjanaboos, P.; Hong, C.K.; Kim, J.H.; Patil, P.S. Symmetric supercapacitor: Sulphurized graphene and ionic liquid. *J. Colloid Interface Sci.* **2018**, *527*, 40–48. [CrossRef] [PubMed]

24.　Wang, T.; Wang, L.X.; Wu, D.L.; Xia, W.; Jia, D.Z. Interaction between nitrogen and sulfur in co-doped graphene and synergetic effect in supercapacitor. *Sci. Rep.* **2015**, *5*, srep09591. [CrossRef]

25.　Wang, H.; Maiyalagan, T.; Wang, X. Review on recent progress in nitrogen-doped graphene: Synthesis, characterization, and its potential applications. *ACS Catal.* **2012**, *2*, 781–794. [CrossRef]

26.　Chen, Y.; Liu, Z.; Sun, L.; Lu, Z.; Zhuo, K. Nitrogen and sulfur co-doped porous graphene aerogel as an efficient electrode material for high performance supercapacitor in ionic liquid electrolyte. *J. Power Sources* **2018**, *390*, 215–223. [CrossRef]

27. Fujisawa, K.; Cruz-Silva, R.; Yang, K.-S.; Kim, Y.A.; Hayashi, T.; Endo, M.; Terrones, M.; Dresselhaus, M.S. Importance of open, heteroatom-decorated edges in chemically doped-graphene for supercapacitor applications. *J. Mater. Chem. A* **2014**, *2*, 9532–9540. [CrossRef]

28. Ji, H.; Hu, S.; Jiang, Z.; Shi, S.; Hou, W.; Yang, G. Directly scalable preparation of sandwiched MoS_2/graphene nanocomposites via ball-milling with excellent electrochemical energy storage performance. *Electrochim. Acta* **2019**, *299*, 143–151. [CrossRef]

29. SaGodse, L.; Karandikar, P.B.; Khaladkar, M.Y. Study of carbon materials and effect of its ball milling, on the capacitance of supercapacitor. *Energy Procedia* **2014**, *54*, 302–309. [CrossRef]

30. Chen, Z.; Hou, L.; Cao, Y.; Tang, Y.; Li, Y. Gram-scale production of B, N co-doped graphene-like carbon for high-performance supercapacitor electrodes. *Appl. Surf. Sci.* **2018**, *435*, 937–944. [CrossRef]

31. Mao, M.; Chen, S.; He, P.; Zhang, H.; Liu, H. Facile and economical mass production of graphene dispersions and flakes. *J. Mater. Chem. A* **2014**, *2*, 4132–4135. [CrossRef]

32. Fernandes, D.M.; Mathumba, P.; Fernandes, A.J.S.; Iwuoha, E.I.; Freire, C. Towards efficient oxygen reduction reaction electrocatalysts through graphene doping. *Electrochim. Acta* **2019**, *319*, 72–81. [CrossRef]

33. Rajkumar, M.; Hsu, C.T.; Wu, T.H.; Chen, M.G.; Hu, C.C. Advanced materials for aqueous supercapacitors in the asymmetric design. *Prog. Nat. Sci. Mater. Int.* **2015**, *25*, 527–544. [CrossRef]

34. Mathumba, P.; Fernandes, D.M.; Matos, R.; Iwuoha, E.I.; Freire, C. Metal Oxide (Co_3O_4 and Mn_3O_4) Impregnation into S, N-doped Graphene for Oxygen Reduction Reaction (ORR). *Materials* **2020**, *13*, 1562. [CrossRef] [PubMed]

35. Ferrari, J.; Robertson, A.C. Interpretation of Raman spectra of disordered and amorphous carbon A. *Phys. Rev. B* **2000**, *61*, 14095–14107. [CrossRef]

36. Fernandes, D.M.; Novais, H.C.; Bacsa, R.; Serp, P.; Bachiller-Baeza, B.; Rodríguez-Ramos, I.; Guerrero-Ruiz, A.; Freire, C. Polyoxotungstate@Carbon Nanocomposites As Oxygen Reduction Reaction (ORR) Electrocatalysts. *Langmuir* **2018**, *34*, 6376–6387. [CrossRef]

37. Farivar, F.; Yap, P.L.; Karunagaran, R.U.; Losic, D. Thermogravimetric Analysis (TGA) of Graphene Materials: Effect of Particle Size of Graphene, Graphene Oxide and Graphite on Thermal Parameters. *J. Carbon Res.* **2021**, *7*, 41. [CrossRef]

38. Limani, N.; Marques, I.S.; Jarrais, B.; Fernandes, A.J.S.; Freire, C.; Fernandes, D.M. Cobalt Phosphotungstate-Based Composites as Bifunctional Electrocatalysts for Oxygen Reactions. *Catalysts* **2022**, *12*, 357. [CrossRef]

39. Yang, S.; Zhi, L.; Tang, K.; Feng, X.; Maier, J.; Müllen, K. Efficient synthesis of heteroatom (N or S)-doped graphene based on ultrathin graphene oxide-porous silica sheets for oxygen reduction reactions. *Adv. Funct. Mater.* **2012**, *22*, 3634–3640. [CrossRef]

40. Wu, D.; Wang, T.; Wang, L.; Jia, D. Hydrothermal synthesis of nitrogen, sulfur co-doped graphene and its high performance in supercapacitor and oxygen reduction reaction. *Microporous Mesoporous Mater.* **2019**, *290*, 109556. [CrossRef]

41. Haque, E.; Zavabeti, A.; Uddin, N.; Wang, Y.; Rahim, A.; Syed, N.; Xu, K.; Jannat, A.; Haque, F.; Zhang, B.Y.; et al. Deciphering the role of quaternary n in O_2 reduction over controlled n-doped carbon catalysts. *Chem. Mater.* **2020**, *32*, 1384–1392. [CrossRef]

42. Zu, C.; Manthiram, A. Hydroxylated graphene-sulfur nanocomposites for high-rate lithium-sulfur batteries. *Adv. Energy Mater.* **2013**, *3*, 1008–1012. [CrossRef]

43. Ai, W.; Luo, Z.; Jiang, J.; Zhu, J.; Du, Z.; Fan, Z.; Xie, L.; Zhang, H.; Huang, W.; Yu, T. Nitrogen and sulfur codoped graphene: Multifunctional electrode materials for high-performance LI-ion batteries and oxygen reduction reaction. *Adv. Mater.* **2014**, *26*, 6186–6192. [CrossRef]

44. Liu, Y.; Qiao, Y.; Wei, G.; Li, S.; Lu, Z.; Wang, X.; Lou, X. Sodium storage mechanism of N, S co-doped nanoporous carbon: Experimental design and theoretical evaluation. *Energy Storage Mater.* **2018**, *11*, 274–281. [CrossRef]

45. Liu, Q.; Zhang, L.; Chen, H.; Jin, J.; Wang, N.; Wang, Y.; Sui, D. Sulfur and nitrogen co-doped three-dimensional graphene aerogels for high-performance supercapacitors: A head to head vertical bicyclic molecule both as pillaring agent and dopant. *Appl. Surf. Sci.* **2021**, *565*, 150453. [CrossRef]

46. Yi, H.T.; Zhu, Y.Q.; Chen, X.Y.; Zhang, Z.J. Nitrogen and sulfur co-doped nanoporous carbon material derived from p-nitrobenzenamine within several minutes and the supercapacitor application. *J. Alloys Compd.* **2015**, *649*, 851–858. [CrossRef]

47. Balaji, S.S.; Raj, A.G.K.; Karnan, M.; Sathish, M. Investigations on the nature of electrolyte on the electrochemical supercapacitor performance of heteroatom doped graphene. *Ionics* **2020**, *26*, 2081–2094. [CrossRef]

48. Tao, B.; Zhang, N.; Ye, T.; Gao, P.; Li, H.; Xie, Y.; Liu, J.; Wang, G.; Zhang, W.; Chang, H. High-voltage aqueous symmetric supercapacitors based on 3D bicontinuous, highly wrinkled, N-doped porous graphene-like ultrathin carbon sheets. *New J. Chem.* **2022**, *46*, 3288–3296. [CrossRef]

49. Xing, L.-B.; Hou, S.-F.; Zhang, J.-L.; Zhou, J.; Li, Z.; Si, W.; Zhuo, S. A facile preparation of three dimensional N, S co-doped graphene hydrogels with thiocarbohydrazide for electrode materials in supercapacitor. *Mater. Lett.* **2015**, *147*, 97–100. [CrossRef]

50. Liu, J.; Zhu, Y.; Chen, X.; Yi, W. Nitrogen, sulfur and phosphorus tri-doped holey graphene oxide as a novel electrode material for application in supercapacitor. *J. Alloys Compd.* **2020**, *815*, 152328. [CrossRef]

51. Besir, M.; Gürsu, H.; Gencten, M.; Sahin, Y. Preparation of different heteroatom doped graphene oxide based electrodes by electrochemical method and their supercapacitor applications. *J. Energy Storage* **2021**, *35*, 102328. [CrossRef]

52. Deng, H.; Zhu, M.; Jin, T.; Cheng, C.; Zheng, J.; Qian, Y. One-step synthesis of nitrogen, sulphur-codoped graphene as electrode material for supercapacitor with excellent cycling stability. *Int. J. Electrochem. Sci.* **2020**, *15*, 16–25. [CrossRef]

53. Abbas, Q.; Raza, R.; Shabbir, I.; Olabi, A.G. Heteroatom doped high porosity carbon nanomaterials as electrodes for energy storage in electrochemical capacitors: A review. *J. Sci. Adv. Mater. Devices* **2019**, *4*, 341–352. [CrossRef]

54. Soysal, M. Voltammetric determination of fenitrothion based on pencil graphite electrode modified with poly(Purpald®). *Chem. Pap.* **2019**, *73*, 1785–1794. [CrossRef]

55. Kesavan, T.; Aswathy, R.; Raj, I.A.; Kumar, T.P.; Ragupathy, P. Nitrogen-Doped Graphene as Electrode Material with Enhanced Energy Density for Next-Generation Supercapacitor Application. *ECS J. Solid State Sci. Technol.* **2015**, *4*, M88–M92. [CrossRef]

56. Liu, Y.-Z.; Li, Y.-F.; Su, F.-Y.; Xie, L.-J.; Kong, Q.-Q.; Li, X.-M.; Gao, J.-G.; Chen, C.-M. Easy one-step synthesis of N-doped graphene for supercapacitors. *Energy Storage Mater.* **2016**, *2*, 69–75. [CrossRef]

57. Jia, S.; Wei, J.; Meng, X.; Shao, Z. Facile and friendly preparation of N/S Co-doped graphene-like carbon nanosheets with hierarchical pore by molten salt for all-solid-state supercapacitor. *Electrochim. Acta* **2020**, *331*, 135338. [CrossRef]

58. Adán-Más, A.; Duarte, R.G.; Silva, T.M.; Guerlou-Demourgues, L.; Montemor, M.F.G. Enhancement of the Ni-Co hydroxide response as Energy Storage Material by Electrochemically Reduced Graphene Oxide. *Electrochim. Acta* **2017**, *240*, 323–340. [CrossRef]

59. Li, Z.; He, W.; Wang, X.; Wang, X.; Song, M.; Zhao, J. N/S dual-doped graphene with high defect density for enhanced supercapacitor properties. *Int. J. Hydrogen Energy* **2020**, *45*, 112–122. [CrossRef]

60. Wu, C.; Cai, J.; Zhu, Y.; Zhang, K. Hybrid Reduced Graphene Oxide Nanosheet Supported Mn-Ni-Co Ternary Oxides for Aqueous Asymmetric Supercapacitors. *ACS Appl. Mater. Interfaces* **2017**, *9*, 19114–19123. [CrossRef] [PubMed]

61. Shams, M.; Guiney, L.M.; Huang, L.; Ramesh, M.; Yang, X.; Hersam, M.C.; Chowdhury, I. Influence of functional groups on the degradation of graphene oxide nanomaterials. *Environ. Sci. Nano* **2019**, *6*, 2203–2214. [CrossRef]

62. Sonia, Y.K.; Meher, S.K. Electrostructural Compatibility of Battery-Type Diffuse-Porous Co_9S_8-$NiCo_2S_4$/Defective Reduced Graphene Oxide and Flaky FeS/Nitrogen-Doped Defective Reduced Graphene Oxide for Ultra-High-Performance All-Solid-State Hybrid Pseudocapacitors. *ACS Appl. Energy Mater.* **2022**, *5*, 13672–13691. [CrossRef]

63. Singh, K.P.; Bhattacharjya, D.; Razmjooei, F.; Yu, J.S. Effect of pristine graphene incorporation on charge storage mechanism of three-dimensional graphene oxide: Superior energy and power density retention. *Sci. Rep.* **2016**, *6*, 31555. [CrossRef] [PubMed]

64. Mandal, B.; Saha, S.; Das, D.; Panda, J.; Das, S.; Sarkar, R.; Tudu, B. Supercapacitor performance of nitrogen doped graphene synthesized via DMF assisted single-step solvothermal method. *FlatChem* **2022**, *34*, 100400. [CrossRef]

65. Fite, M.C.; Imae, T. Capacitance enhancement of nitrogen-doped graphene oxide/magnetite with polyaniline or carbon dots under external magnetic field: Supported by theoretical estimation. *J. Colloid Interface Sci.* **2021**, *594*, 228–244. [CrossRef] [PubMed]

66. Zhang, S.; Sui, L.; Dong, H.; He, W.; Dong, L.; Yu, L. High-Performance Supercapacitor of Graphene Quantum Dots with Uniform Sizes. *ACS Appl. Mater. Interfaces* **2018**, *10*, 12983–12991. [CrossRef]

67. Kumar, A.; Tan, C.-S.; Kumar, N.; Singh, P.; Sharma, Y.; Leu, J.; Huang, E.-W.; Winie, T.; Wei, K.-H.; Tseng, T.Y. Pentafluoropyridine functionalized novel heteroatom-doped with hierarchical porous 3D cross-linked graphene for supercapacitor applications. *RSC Adv.* **2021**, *11*, 26892–26907. [CrossRef]

68. Zhou, J.; Shen, H.; Li, Z.; Zhang, S.; Zhao, Y.; Bi, X.; Wang, Y.; Cui, H.; Zhuo, S. Porous carbon materials with dual N, S-doping and uniform ultra-microporosity for high performance supercapacitors. *Electrochim. Acta* **2016**, *209*, 557–564. [CrossRef]

69. Torchała, K.; Kierzek, K.; Machnikowski, J. Capacitance behavior of KOH activated mesocarbon microbeads in different aqueous electrolytes. *Electrochim. Acta* **2012**, *86*, 260–267. [CrossRef]

70. Zhou, W.; Lei, S.; Sun, S.; Ou, X.; Fu, Q.; Xu, Y.; Xiao, Y.; Cheng, B. From weed to multi-heteroatom-doped honeycomb-like porous carbon for advanced supercapacitors: A gelatinization-controlled one-step carbonization. *J. Power Sources* **2018**, *402*, 203–212. [CrossRef]

71. Gopalakrishnan, A.; Badhulika, S. From onion skin waste to multi-heteroatom self-doped highly wrinkled porous carbon nanosheets for high-performance supercapacitor device. *J. Energy Storage* **2021**, *38*, 102533. [CrossRef]